APPLIED PHYSICS

Nuclear quadrupole resonance spectroscopy with a femtotesla diamond magnetometer

Yaser Silani[1], Janis Smits[1], Ilja Fescenko[1,2], Michael W. Malone[3], Andrew F. McDowell[4], Andrey Jarmola[5,6], Pauli Kehayias[7], Bryan A. Richards[1], Nazanin Mosavian[1], Nathaniel Ristoff[1], Victor M. Acosta[1]*

Radio frequency (RF) magnetometers based on nitrogen vacancy centers in diamond are predicted to offer femtotesla sensitivity, but previous experiments were limited to the picotesla level. We demonstrate a femtotesla RF magnetometer using a diamond membrane inserted between ferrite flux concentrators. The device provides ~300-fold amplitude enhancement for RF magnetic fields from 70 kHz to 3.6 MHz, and the sensitivity reaches ~70 fT $\sqrt{s}$ at 0.35 MHz. The sensor detected the 3.6-MHz nuclear quadrupole resonance (NQR) of room-temperature sodium nitrite powder. The sensor's recovery time after an RF pulse is ~35 μs, limited by the excitation coil's ring-down time. The sodium-nitrite NQR frequency shifts with temperature as −1.00±0.02 kHz/K, the magnetization dephasing time is T_2^*=887±51 μs, and multipulse sequences extend the signal lifetime to 332±23 ms, all consistent with coil-based studies. Our results expand the sensitivity frontier of diamond magnetometers to the femtotesla range, with potential applications in security, medical imaging, and materials science.

INTRODUCTION

Magnetometers based on negatively charged nitrogen vacancy (NV) centers in diamond are promising room-temperature sensors for detecting magnetic phenomena across a wide range of frequencies (*1*). Over the past decade, various sensing protocols and fabrication methods have been developed to improve the sensitivity of diamond magnetometers in the sub–10-kHz (*2*–*5*), radio frequency (RF) (*6*–*8*), and microwave (MW) (*9*, *10*) frequency ranges. However, the best reported sensitivities, ~1 pT $s^{1/2}$ (*3*), still trail the achievable levels in magnetometers based on alkali-metal vapor (*11*–*17*) and superconducting quantum interference devices (*18*–*20*).

Recently, magnetic flux concentrators have been used to improve the performance of diamond magnetometers (*3*, *5*, *21*, *22*), and a sub-picotesla sensitivity has been realized for low frequencies ($\lesssim$1 kHz) by inserting an NV-doped diamond membrane between two ferrite cones (*3*). We hypothesized that the same approach can be used for improving the sensitivity in the RF range (kilohertz to megahertz) if the flux concentrator's magnetic properties do not degrade at such frequencies. In fact, better sensitivity may be expected in the RF range because the diamond RF magnetometer can operate in a pulsed regime where the NV spin coherence time is substantially longer (*23*).

A diamond RF magnetometer with femtotesla sensitivity may find immediate application as a noninductive detector for nuclear quadrupole resonance (NQR) spectroscopy (*24*–*26*). NQR spectroscopy is a solid-state analysis technique that provides a unique chemical fingerprint based on the coupling of nuclear quadrupole moments to their local electric field gradients (*27*, *28*). NQR spectroscopy is used to identify powder substances in ambient conditions for security (*29*–*31*) and pharmaceutical (*32*–*34*) applications and to study the temperature-dependent properties of single-crystal materials (*35*–*39*). These applications typically require the ability to detect kilohertz to megahertz frequencies, at low-bias magnetic fields $\lesssim$1 mT, with femtotesla sensitivity (*40*). Previously, NV centers were used to detect NQR signals arising from nanoscale statistical polarization in single-crystal boron nitride layers in direct contact with the diamond (*41*, *42*). However, using NV centers to remotely detect powders remains an open challenge due to the need for high sensitivity (*43*).

Here, we demonstrate a frequency-tunable diamond RF magnetometer with a sensitivity of ~70 fT $s^{1/2}$ at 0.35 MHz, using ferrite flux concentrators (*3*) and a multipulse synchronized readout scheme (*7*, *8*). The sensitivity remains within a factor of three of this value for the frequency range of 0.07 to 3.6 MHz. We used the magnetometer to detect the 3.6-MHz NQR signal of ^{14}N in sodium nitrite powder samples (*44*, *45*). Our work expands the sensitivity frontier of diamond magnetometry to the femtotesla range and introduces a new method for remote detection of solid-state magnetic resonance.

RESULTS

Experimental design

A schematic of the diamond RF magnetometer is shown in Fig. 1A. The apparatus is similar to one previously used for low-frequency magnetometry (*3*), with modifications (Materials and Methods and section S1) made for RF magnetometry and NQR spectroscopy. For example, the mu-metal shield is replaced by an aluminum shield to suppress RF interference. A thermal insulation housing with thermoelectric temperature control is added around the shield to improve thermal stability. Calibrated RF test fields with a magnitude B_{test} and frequency f_{test} are applied along the magnetometer sensing axis (z axis) using a pair of low-inductance rectangular wire loops.

A permanent magnet is used to compensate the ambient magnetic field and apply a weak bias field, B_0 = 2 μT to 15 μT,

[1]Center for High Technology Materials and Department of Physics and Astronomy, University of New Mexico, Albuquerque, NM, USA. [2]Laser Centre, University of Latvia, Riga, Latvia. [3]Los Alamos National Laboratory, Los Alamos, NM, USA. [4]NuevoMR, Albuquerque, NM, USA. [5]ODMR Technologies Inc., El Cerrito, CA, USA. [6]Department of Physics, University of California, Berkeley, Berkeley, CA, USA. [7]Sandia National Laboratories, Albuquerque, NM, USA.
*Corresponding author. Email: vmacosta@unm.edu

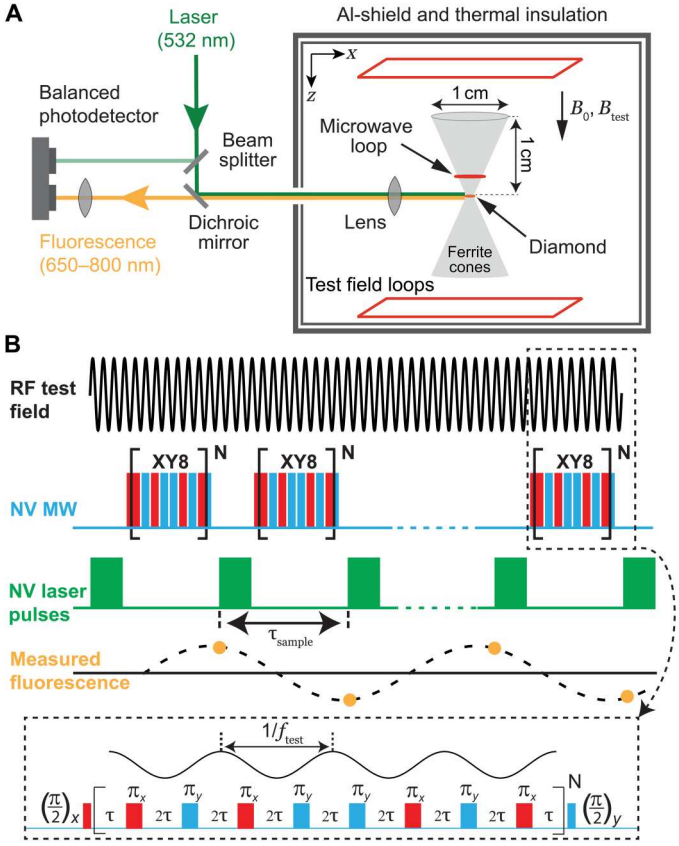

Fig. 1. Experimental setup and RF detection scheme. (**A**) Schematic of the experimental setup for detecting RF test fields. A permanent magnet (not shown) outside the Al shield was used to apply weak bias magnetic fields along the *z* axis, B_0 = 2 μT to 15 μT. Additional details of the setup can be found in Materials and Methods, section S1, and (*3*). (**B**) Diamond RF magnetometry is performed with a continuous series of repeated XY8-*N* pulse sequences on the NV electron spins (*8*). Each XY8-*N* sequence begins and ends with a resonant MW π/2 pulse. Between the π/2 pulses, 8*N* resonant π-pulses, spaced by $2\tau = 1/(2f_{test})$, are applied with alternating phase. Following each XY8-*N* sequence, a 12-μs laser pulse (0.2 W and 532 nm) is applied for optical readout and repolarization of the NV centers. The resulting time trace of NV fluorescence readouts is proportional to an aliased version of the RF test field.

approximately along the *z* axis. The flux concentrators enhance the *z* component of the magnetic field in the gap between the cone tips. An NV-doped diamond membrane is positioned in the gap with its (100) crystal faces normal to the *z* axis. This geometry results in two NV spin transition frequencies $f_{\pm} \approx D \pm \varepsilon\gamma_{nv}B_0/\sqrt{3}$, where D = 2.87 GHz is the NV zero field splitting, ε is the flux-concentrator enhancement factor (ε ≈ 300 for DC fields) (*3*), γ_{nv} = 28 GHz/T is the NV gyromagnetic ratio, and the factor of $\sqrt{3}$ comes from the 55° angle of each NV axis with respect to the *z* axis.

Figure 1B shows the XY8-*N* synchronized readout pulse sequence used for diamond RF magnetometry (*8*). This pulse sequence contains a series of short MW pulses (10 to 70 ns), of alternating phase, that are tuned to one of the $f_{\pm}$ resonances in the range of 2.7 to 3.0 GHz. Each XY8-*N* sequence is followed by a 12-μs laser pulse (0.2 W and 532 nm), generated with an acousto-optic modulator, for optical readout and spin polarization of the NV centers. The sequence is repeated continuously, and the resulting time trace of NV fluorescence readouts is approximately proportional to an aliased version of the applied RF field sampled at the time of the first π/2 pulse of each XY8-*N* sequence (section S2a). For a magnetic field oscillating with frequency *f*, the NV fluorescence signal oscillates with an alias frequency $f_{alias} = f - f_{ref}$. The reference frequency, f_{ref}, depends on the sampling rate $1/\tau_{sample}$, which is adjusted by varying a sub-microsecond dead time after each XY8-*N* sequence (*8*).

A theoretical bound on the diamond RF magnetometer sensitivity is set by photoelectron shot noise as

$$\eta_{psn} \approx \frac{\sqrt{3}}{\varepsilon}\frac{\xi}{\sqrt{\delta}}\frac{1}{4\,\gamma_{nv}\,C\sqrt{n_{nv}\,V_{sen}\,\phi\,\tau_{tot}}} \quad (1)$$

In the first term of Eq. 1, the $\sqrt{3}$ factor comes from the 55° angle of each NV axis with respect to the *z* axis, ξ = 1.6 accounts for additional photoelectron noise arising from the balanced detection and normalization procedure (section S2a), and $\delta = \tau_{tot}/\tau_{sample} \approx 0.75$ is a duty cycle, where τ_{tot} is the NV phase accumulation time and τ_{sample} is the sequence repetition time. In the second term, C is the XY8-*N* fluorescence contrast (section S2a), n_{nv} is the NV concentration, V_{sen} is the illuminated NV sensor volume, and ϕ is the probability of detecting a photoelectron per NV center for a single readout.

The natural-isotopic-abundance single-crystal diamond membrane used in this work contained an initial nitrogen concentration of ~20 parts per million (ppm). The diamond was doped with NV centers by electron irradiation and annealing (Materials and Methods), resulting in an NV concentration of $n_{nv} \approx 3$ ppm and a transverse NV spin coherence time of ~50 μs for an XY8-4 sequence. The diamond was subsequently cut and polished into a (100)-oriented membrane with dimensions ~300 μm by 300 μm by 35 μm. The NV sensor volume is defined by the area of the illuminating laser beam and the length of its path in the diamond as $V_{sen} \approx 3 \times 10^5$ μm^3. The peak detected photoelectron current was typically ~0.17 mA over a 2-μs readout window, which indicates that the detection efficiency of our setup is $\phi \approx 0.02$. We found the best sensitivity of our setup to occur for XY8-4 sequences at f_{test} = 0.35 MHz, where τ_{tot} = 44 μs and $C \approx 0.01$. With these values and assuming that the flux-concentrator enhancement factor ε ≈ 300 is the same as for DC fields, Eq. 1 predicts a photoelectron shot noise–limited sensitivity $\eta_{psn} \approx 30$ fT s$^{1/2}$.

Magnetometer characterization

We measured the magnetometer's sensitivity as a function of test field frequency and acquisition time. First, we applied a test field with frequency f_{test} = 0.35 MHz and magnitude B_{test} = 100 pT$_{rms}$ (section S3a) and recorded the magnetometer signal under an XY8-4 synchronized readout sequence for 100 s with and without the ferrite cones. Figure 2A shows the real-time NV fluorescence signal for a segment of each time trace. While the magnetometer signal without ferrite cones is dominated by noise, a clear oscillation at frequency $f_{test} - f_{ref}$ = 3.5 kHz is observed with the cones present.

To determine the magnetometer sensitivity, each 100-s NV time trace is divided into 100 1-s segments; a spectrum is obtained for each segment by taking the absolute value of the Fourier transform, and the 100 spectra are averaged together. Figure 2B shows the resulting magnetic spectra for the recordings with and without the ferrite cones. The magnetic field sensitivity, defined here as the

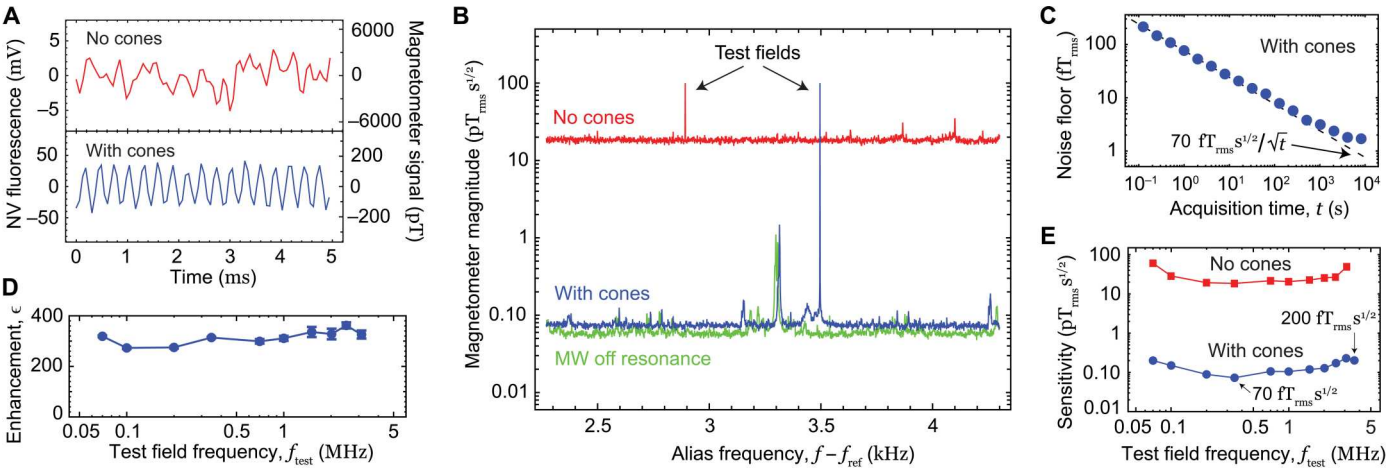

Fig. 2. Femtotesla diamond RF magnetometry. (**A**) Real-time NV fluorescence signal with (blue) and without (red) ferrite cones in the magnetometer assembly. In each case, an XY8-4 synchronized readout sequence was used, and a 0.35-MHz test field with 100 pT$_{rms}$ amplitude was applied. The NV fluorescence photodetector voltage is converted to magnetic field units using the procedure described in section S3a. For the same applied field amplitude, the photodetector voltage signal with cones is ~220 times larger than that without cones, primarily because of the flux concentrator enhancement (and, to a lesser extent, differences in the photon collection efficiency). A digital 4.5-kHz low-pass filter was applied to the data without cones for better visualization. (**B**) Fourier transform spectra of the NV signals with and without the cones. No digital filtering was applied. The noise floor reaches ~70 fT s$^{1/2}$ with the cones and ~18 pT s$^{1/2}$ without them. A reference spectrum (green), obtained by detuning the MW frequency 200 MHz off the NV resonance, shows an effective noise floor of ~60 fT s$^{1/2}$. Peaks due to the test field appear prominently, but there are several smaller peaks in the spectra. The features that are absent in the MW off resonance spectrum are likely from magnetic noise. The remaining features are of unknown origin (section S4). (**C**) Noise floor with the cones present as a function of acquisition time, t. (**D**) Ferrite cone enhancement factor versus the test field frequency (section S3b). (**E**) Diamond RF magnetometer sensitivity as a function of test field frequency with (blue circles) and without (red squares) the ferrite cones (section S4). For all data in this figure, except for the "MW off resonance" spectrum in (B), the MW frequency was tuned to one of the NV $f_{\pm}$ resonances.

average noise floor for 1-s acquisition time in a few-hundred-hertz band near the signal frequency (section S4), is ~70 fT$_{rms}$ s$^{1/2}$ with the cones and ~18 pT$_{rms}$ s$^{1/2}$ without them. A reference spectrum (with ferrite cones) was obtained by detuning the MW frequency 200 MHz off the NV resonance, revealing an effective noise floor of ~60 fT$_{rms}$ s$^{1/2}$. While the ~70 fT$_{rms}$ s$^{1/2}$ measured noise floor with ferrite cones is about two times greater than the photoelectron shot noise estimate (section S2b), the experimental sensitivity represents a ≳10-fold improvement over previous diamond magnetometry studies (*3*) and a ≳100-fold improvement over previous diamond studies in the RF range (*6*–*8*).

To characterize temporal stability, we continuously recorded the ferrite-cone diamond RF magnetometer signal for several hours. Figure 2C shows the magnetic noise floor as a function of averaging time, t. We find that the noise floor scales with the expected ~ 70 fT s$^{1/2}$/$\sqrt{t}$ behavior out to $t \gtrsim 10^3$ s. The noise floor decreases to below 2 fT after 1 hour of acquisition, before leveling off.

We used ferrite cones made of a manganese-zinc material (MN60) that is usually considered more suitable for low-frequency (≲1 MHz) applications (*46*), and it was initially unclear whether large enhancement factors would be possible at higher frequency (*47*). To probe the frequency dependence, we recorded the diamond RF magnetometer signal for different values of f_{test}. The enhancement factor provided by the ferrite cones is defined as $\varepsilon = B_{gap}/B_{test}$, where B_{gap} is the magnetic field amplitude within the diamond when the cones are present. For each value of f_{test}, we calibrated B_{test} by recording the NV signal amplitude (without cones) as a function of the current amplitude applied to the test field loops. We repeated the process with the cones present to calibrate B_{gap}. At each frequency, ε was estimated from the ratio of the response curves (section S3b). The results are shown in Fig. 2D. Unexpectedly, we find that the enhancement factor is nearly constant (ε ≈ 300) in the frequency range of 0.07 to 3.12 MHz.

We also determined the magnetic sensitivity as a function of frequency using the process described for Fig. 2 (A and B). Figure 2E shows the sensitivity as a function of f_{test}. For each frequency, the duration and spacing of the MW pulses, and the length of the XY8-N sequence were modified to maximize sensitivity (see table S2 and section S4). With the cones, the best sensitivity is ~70 fT s$^{1/2}$ at f_{test} = 0.35 MHz, and the sensitivity remains within a factor of 3 of this value throughout the range of 0.07 to 3.62 MHz. A diamond with a lower nitrogen concentration, and thus longer coherence time, can be used to extend the frequency range down to ~1 kHz (*1*). A stronger MW field, combined with a higher-NV-concentration diamond (to limit the number of MW pulses without sacrificing sensitivity), could extend the frequency up to ≳10 MHz, as long as the ferrite's permeability and relative loss factor do not degrade (*3*).

NQR spectroscopy of $NaNO_2$ powder: Experimental design and theoretical estimates

Having demonstrated femtotesla sensitivity in the RF range, we next used our ferrite-cone diamond RF magnetometer as a detector in NQR spectroscopy. The sample that we selected to study is sodium nitrite ($NaNO_2$) powder (Materials and Methods), a well-studied standard for ^{14}N NQR spectroscopy (*48*, *49*). Figure 3A shows a schematic of the NQR detection setup. A resonant RF coil is wrapped around a $NaNO_2$ powder sample, and the sample is placed ~4 mm above the ferrite-cone diamond RF magnetometer. Two-coil assemblies are used: one for a 4-g sample and the other for a 21-g sample. A capacitor tuning circuit and pi-network are used for conventional inductive detection (section S5c).

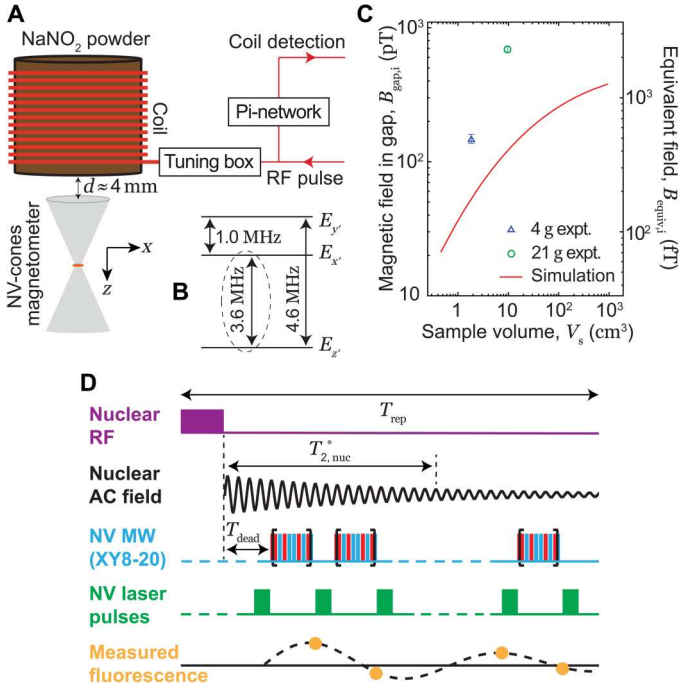

Fig. 3. NQR setup. (**A**) Schematic of the setup used for NQR spectroscopy. A bias field $B_0 \approx 15$ μT is applied along the z axis. A $NaNO_2$ sample is housed in a plastic cylinder container and placed $d \approx 4$ mm above the ferrite-cone diamond RF magnetometer. A resonant RF coil is wrapped around the sample container. The 3.6-MHz NQR transition of ^{14}N nuclei in $NaNO_2$ is excited by applying RF pulses along the z axis. The resulting oscillating nuclear magnetic field is also along the z axis and is simultaneously detected by the ferrite-cone diamond RF magnetometer and the resonant RF coil (see section S5c). (**B**) Energy levels and nuclear spin transitions of ^{14}N in $NaNO_2$ at room temperature and low (≲1 mT) magnetic field. (**C**) Initial magnetic field amplitude within the diamond, $B_{gap,i}$ (left axis), and equivalent magnetic field, $B_{equiv,i} = B_{gap,i}/300$ (right axis), as a function of sample volume. Expt., experiment. (**D**) Pulse sequence used for NV NQR detection (section S5a). After an RF excitation pulse, an XY8-20 synchronized readout pulse sequence is used to detect an aliased version of the nuclear AC magnetic field. The entire sequence is repeated every $T_{rep} = 0.5$ s.

The nuclear quadrupole Hamiltonian is given by (*50*)

$$H_Q = f_Q \left[I_{z'}^2 + \frac{\eta}{3}(I_{x'}^2 - I_{y'}^2) \right] \quad (2)$$

where f_Q is the quadrupole coupling frequency, η is the asymmetry parameter, and $\{I_{x'}, I_{y'}, I_{z'}\}$ are the spin components along the principle axes of a given crystallite. As depicted in Fig. 3B, at low magnetic field ($B_0 \lesssim 1$ mT), the ^{14}N nucleus in $NaNO_2$ ($I = 1$, $f_Q = 4.1$ MHz, $\eta = 0.38$) has three nondegenerate energy levels, $\{E_{z'}, E_{x'}, E_{y'}\}$, and magnetic-dipole transitions are allowed between each level (*44*). We used our sensor to detect the $E_{z'} \leftrightarrow E_{x'}$ transition at $f_{nqr} = f_Q(1 - \eta/3) = 3.6$ MHz. For powder samples, where many crystallites are randomly oriented, application of a resonant RF pulse along the z axis produces a net oscillating magnetization (frequency f_{nqr}) along the z axis (see section S6) (*51*). Thus, to maximize the NQR signal, the RF coil axis was aligned with the magnetometer detection axis (Fig. 3A).

We carried out simulations to estimate the oscillating magnetic field amplitude produced by cylindrical $NaNO_2$ samples following an optimal RF excitation pulse on the 3.6-MHz transition. The initial amplitude of the oscillating sample magnetization was estimated to be $M_0 = 3.3$ μA/m along the z axis (see section S6). A finite-element model was used to make a preliminary estimate of the resulting initial magnetic field amplitude in the diamond when the ferrite cones were present, $B_{gap,i}$. For this and all subsequent NQR measurements, B_{gap} is converted to an equivalent magnetic field $B_{equiv} = B_{gap}/\varepsilon$, using $\varepsilon = 300$ (see section S3b), to compare with the case of uniform magnetic fields.

For a given sample volume V_s, we swept the cylinder aspect ratio to estimate the maximum possible nuclear field amplitude (section S7). Figure 3C shows the maximum simulated $B_{equiv,i}$ as a function of sample volume. The estimated $B_{equiv,i}$ values are at the few-hundred femtotesla level for the $V_s = 1 - 10^3$ cm^3 range. Figure 3C also shows experimentally measured NQR signals from two sample masses (these measurements are described below). The experimental values are three to six times larger than the simulated estimates despite several optimistic assumptions such as perfect powder packing, optimal RF excitation pulse, and ideal sample aspect ratio. As discussed below, this difference is due to signal amplification from the resonant RF coil used in the experiment.

Figure 3D shows the pulse sequence used for NQR spectroscopy. RF excitation pulses (typically 50 to 200 μs) are applied to the resonant RF coil, and the oscillating nuclear magnetic field is detected by the diamond RF magnetometer using a series of repeated XY8-20 pulse sequences with $f_{ref} = 3600.07$ kHz. After a duration $T_{rep} \approx 0.5$ s, chosen to be comparable to the ^{14}N thermal relaxation time, $T_{1,nuc} \approx 0.3$ s (*45*), the entire sequence is repeated. To compare to conventional NQR detection, the same coil is also used to detect the signal inductively after it is passed through a pi-network and amplified by a low-noise preamplifier (see Fig. 3A and section S5c).

NQR detection with a single RF pulse

Figure 4A shows the NQR signals of the 21-g $NaNO_2$ powder sample detected by the resonant RF coil and ferrite-cone diamond RF magnetometer. The signals are fit with exponentially decaying sinusoidal functions, and the fitted $1/e$ decay times are $T^*_{2,nuc} = 844 \pm 13$ μs for the coil signal and $T^*_{2,nuc} = 887 \pm 51$ μs for the NV signal. These values are in good agreement with each other and consistent with literature values (*45*).

The NV signal in Fig. 4A has an initial amplitude $B_{equiv,i} = 2300 \pm 115$ fT, which is a factor of 6 higher than the simulation in Fig. 3C. The discrepancy comes from induction in the resonant RF coil wrapped around the sample in the experiment (*52*, *53*). The oscillating sample magnetization induces an oscillating current in the coil. The current is resonantly amplified and produces a larger oscillating field with a phase shift. This AC magnetic field can be described as arising from an effective magnetization throughout the resonant RF coil

$$M_{eff} \approx Q \frac{m_s}{V_c \rho_s} M_0 \quad (3)$$

where $Q \gg 1$ is the coil's quality factor, V_c is the coil volume, m_s is the sample mass, ρ_s is the sample's crystal density, and M_0 is the initial amplitude of the oscillating sample magnetization. Taking the parameters used for the experiments in Fig. 4 ($Q = 23$, $V_c = 20$ cm^3, $m_s = 21$ g, $\rho_s = 2.17$ g/cm^3) and assuming the maximum initial magnetization, $M_0 = 3.3$ μA/m (section S6), we find $M_{eff} \approx 37$ μA/m. We used the finite-element model to evaluate the

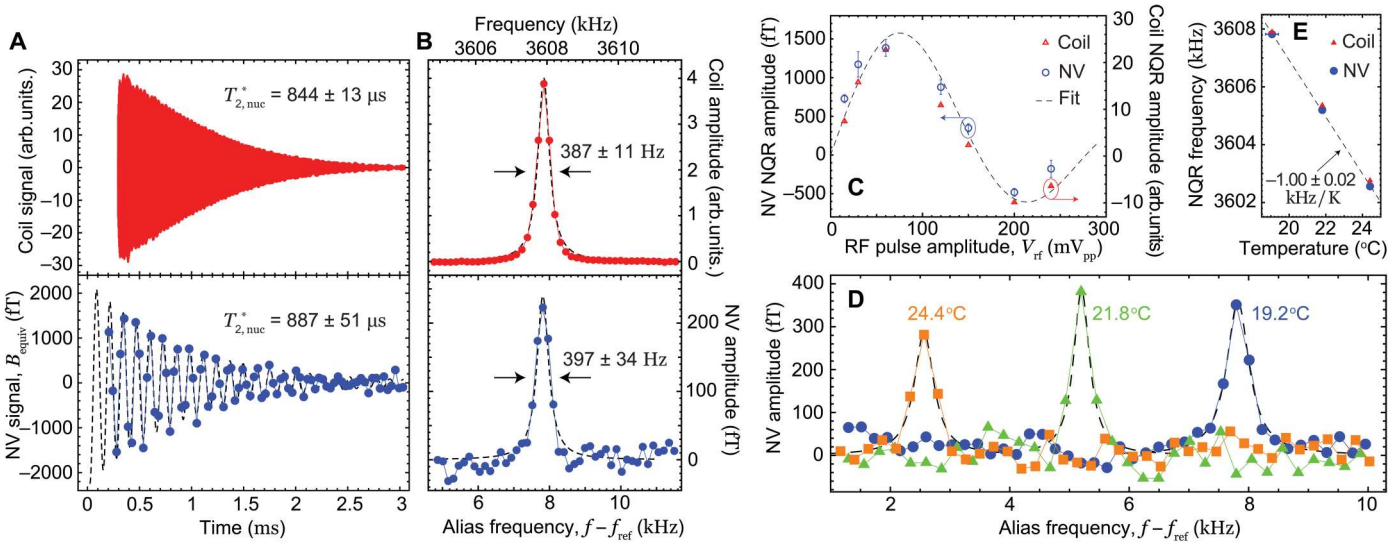

Fig. 4. NQR spectroscopy of ^{14}N in $NaNO_2$. (**A**) Room-temperature time-domain NQR signal of ^{14}N in a 21-g $NaNO_2$ powder sample acquired by the resonant RF coil (top) and diamond RF magnetometer (bottom). A 50-μs RF pulse at 3605 kHz was used to excite the sample via the resonant RF coil with loaded quality factor $Q \approx 23$ (see section S5c). The sequence was repeated every 500 ms, and the signal was averaged over 86,000 repetitions. A digital band-pass filter is applied for better visualization: 3.58 to 3.63 MHz for the coil signal and 4.6 to 11.7 kHz for the NV signal. (**B**) Imaginary part of the Fourier transform of the time-domain NQR signals shown in (A), along with Lorentzian fits. (**C**) NQR signal amplitude as a function of RF pulse amplitude, V_{rf} (measured in volts, before amplification), applied at 3607.5 kHz for 300 μs. For each RF pulse amplitude, the imaginary part of the Fourier transform of the first 810 μs of the signals is calculated such that the NQR resonance is contained in a single frequency point. The value of that point is taken as the NQR amplitude, and the error bars are the SD of points within a 5-kHz band near resonance. The dashed black line is a fit to a function $J_{3/2}(\alpha)/\sqrt{\alpha}$ with the first peak occurring at the nutation angle $\alpha = 119°$ (*49*, *54*). (**D**) NV NQR spectra (imaginary part of Fourier transform) obtained for three different ambient temperatures, along with Lorentzian fits. RF pulses were applied at 3605 kHz for 50 μs. (**E**) NQR resonance frequency as a function of ambient temperature, along with linear fit.

magnetic field within the diamond, assuming that M_{eff} is uniform throughout the excitation coil volume (section S7). After converting to the effective magnetic field, the estimated initial amplitude is $B_{equiv,i} \approx 3100$ fT. This is only a factor of ~1.35 larger than the experimental value, and the remaining difference may be due to imperfect RF excitation.

Figure 4B shows the NQR frequency spectra detected by both coil and NV sensors along with Lorentzian fits. For the NV NQR spectrum, the fitted resonance frequency is $f_{nqr} = f_{alias} + f_{ref} = 3607.883 \pm 0.013$ kHz, which is in reasonable agreement with the fitted coil–detected NQR frequency of 3607.908 ± 0.004 kHz.

Figure 4C shows the NQR signal amplitude as a function of the RF pulse amplitude V_{rf}, for a pulse length $t_{rf} = 300$ μs. The signal amplitude is well described by the function $S_{nqr}(V_{rf}) = S_{max}\, J_{3/2}(\alpha)/(0.436\ \sqrt{2\alpha/\pi})$ [see (*54*) and section S6], where $J_{3/2}$ is the Bessel function of order 3/2, $\alpha = 2\pi\gamma_n K V_{rf} t_{rf}$ is the nutation angle, γ_n is the nuclear spin gyromagnetic ratio, and $KV_{rf} = B_{rf}$ is the applied RF magnetic field amplitude with fitted conversion factor K (section S5b). The maximum signal amplitude, S_{max}, occurs following an RF excitation pulse with $\alpha \approx 2.08$ rad = 119° (*49*, *54*).

Temperature dependence of NQR frequency

The temperature dependence of NQR frequencies provides insight into crystal structure (*35*–*39*), and it can be used to validate the interpretation of spectra. We studied the temperature dependence of the 3.6-MHz $NaNO_2$ NQR transition near room temperature by controlling the apparatus temperature with a Peltier element and measuring the ambient temperature with a thermistor located near the sample (Materials and Methods). Figure 4D shows the NV NQR spectrum for three different temperatures. Each ~2.6-K step in temperature leads to a shift of the resonance of several linewidths. The NQR central frequencies are plotted as a function of temperature in Fig. 4E. A linear fit yields the coefficient −1.00 ± 0.02 kHz/K, which is consistent with previous measurements near room temperature (*44*, *45*, *55*).

Sensor recovery time following an RF pulse

To detect NQR signals from samples with short dephasing times (*25*, *26*), a sensor with a short recovery time following an RF excitation pulse is desired. For inductive detection, the recovery time is determined by the resonant RF coil's ring-down, and it can be ≪100 μs for low-Q coils. However, some noninductive detectors such as alkali-metal vapor magnetometers have substantially longer recovery times, ≳1 ms (*15*, *26*). We hypothesized that the NV sensor's recovery time should be limited by either the coil ring-down or the NV polarization time (12 μs in our experiment), whichever is longer. To measure the recovery time, we used a 4-g $NaNO_2$ powder sample and a resonant RF coil with a loaded quality factor $Q \approx 8$ (section S5c). The smaller sample and lower Q were chosen to test the limits of mass sensitivity and recovery time of our apparatus. Figure 5A shows the time-domain NV NQR signal following a 200-μs RF pulse ($\alpha \approx 119°$). Figure 5B shows the Fourier transform spectrum for three different "deadtimes," computed by dropping the corresponding initial data points from the time-domain data in Fig. 5A. For a deadtime of ~35 μs, the NQR peak is still prominent above the background. The coil-detected signal exhibits a similar recovery time, suggesting that this time scale is

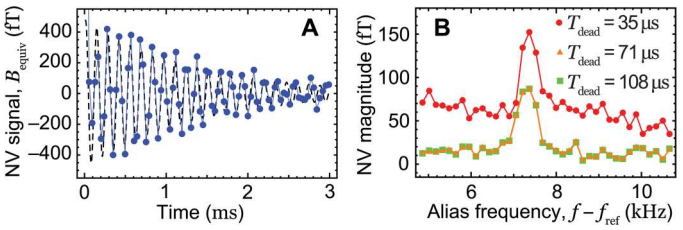

Fig. 5. NV NQR recovery time. (**A**) Time-domain NV NQR signal of 4 g of $NaNO_2$ powder enclosed in a $Q \approx 8$ resonant RF coil. The RF pulse was applied at 3608 kHz for 200 μs. A digital band-pass filter (4.7 to 10.8 kHz) was applied for better visualization. (**B**) NV NQR spectrum (absolute value of Fourier transform) for three different deadtimes. T_{dead} is defined in Fig. 3D.

limited by the coil ring-down time and not by properties of the NV centers.

The initial amplitude in Fig. 5A, $B_{equiv,i} = 495 \pm 38$ fT, is consistent with a modest amplification due to the resonant RF coil. Using Eq. 3 and correcting for the coil standoff from the sensor, the upper bound on the initial signal amplitude from the 4-g sample is $B_{equiv,i} \approx 760$ fT (section S7), which is only a factor of ~1.5 larger than the experimental value.

Spin-lock spin-echo spectroscopy

Nuclear spins in most room-temperature solids have the property $T^*_{2,nuc} \ll T_{1,nuc}$. This implies a low duty cycle for NQR readout because $T^*_{2,nuc}$ limits the spin-precession acquisition time and $T_{1,nuc}$ bounds the rethermalization time needed to repeat the sequence. One technique to increase the NQR readout duty cycle is to apply a spin-lock spin-echo (SLSE) pulse sequence (*56*). In SLSE, Fig. 6A, a series of phase-synchronized RF pulses are applied to extend the lifetime of the NQR signal out to a time $T_2^{SLSE} \gg T^*_{2,nuc}$. Each echo pulse resets the phase of the nuclear spin precession such that the NQR signals following each pulse can be coherently averaged together (*56*–*58*). Figure 6 (B and C) shows the NV-detected time-domain and frequency-domain SLSE signals from the 21-g sample averaged over the first 20 echos. A clear resonance at the expected NQR frequency ($f_{alias} + f_{ref} = 3606.7$ kHz) is observed. Figure 6D shows the SLSE signal magnitude as a function of time since the first RF pulse. A fit to a single exponential decay reveals $T_2^{SLSE} = 332 \pm 23$ ms, a time scale that is consistent with previous studies (*56*, *59*). Figure 6E shows the SLSE signal-to-noise ratio (SNR) as a function of the total experimental acquisition time, t. The SNR of the single–RF pulse measurement in Fig. 4 is also shown for comparison. In both cases, the SNR scales as $\sqrt{t}$, but the SLSE SNR is about three times greater. This is due to a combination of factors: The SLSE data has a approximately threefold smaller NQR signal amplitude, but it has more than an order of magnitude higher readout duty cycle, and there was some additional RF noise in the single-pulse data that was not present in the SLSE measurement (section S8).

DISCUSSION

While this work realizes several benchmarks in the development of diamond quantum sensors, the present implementation of RF magnetometry and NQR detection operates far from fundamental limits.

Optimizing the diamond RF magnetometer

The diamond RF magnetometer sensitivity could be improved by illuminating a greater fraction of the diamond (*60*), increasing the fluorescence collection efficiency (*61*, *62*), optimizing the MW pulse sequence (*63*, *64*), and increasing the flux concentrator enhancement factor (*3*). Each of these improvements could plausibly provide a ≳3-fold improvement in sensitivity and together might allow a sensitivity ≲1 fT $s^{1/2}$, provided that the flux concentrator's magnetic noise remains sufficiently low (*65*). Magnetic fields from localized samples may also be further enhanced by providing an additional flux return path using a closed cylinder or C-shaped ferrite clamp (*66*).

Johnson noise and comparison of coil and diamond NQR detectors

To improve NQR detection, it is tempting to leverage the resonant-induction amplification method introduced here and increase the coil Q (see Eq. 3). However, the Johnson noise in the coil is also resonantly amplified and must be considered. The root mean square (rms) Johnson magnetic noise inside an impedance-matched solenoidal coil on resonance (*52*) is

$$\eta_J \approx \sqrt{\frac{2\, k_B\, T\, \mu_c\, Q}{\pi\, f_0\, V_c}} \tag{4}$$

where k_B is the Boltzmann constant, T is the temperature, μ_c is the permeability inside the coil, and f_0 is the coil's resonance frequency. When using a high-Q RF coil wrapped around the sample, the SNR of NQR detection is fundamentally limited by Johnson noise, regardless of the mode of detection. Assuming $f_0 = f_{nqr}$ and $\mu_c = \mu_0$, where μ_0 is the vacuum permeability, and neglecting nuclear-spin dephasing and experimental dead times, the Johnson-noise–limited SNR is given by Eqs. 3 and 4 as (*67*)

$$SNR_J \approx \sqrt{\frac{\pi \mu_0 Q f_{nqr}}{4 V_c k_B T}} \frac{m_s}{\rho_s} M_0 \tag{5}$$

Using parameters from the experiment (section S5c), we find $SNR_J \approx 210$ $Hz^{1/2}$ for the 4-g coil and $SNR_J \approx 1020$ $Hz^{1/2}$ for the 21-g coil. These values are about two orders of magnitude higher than the SNR in our experiments (section S9a), but they represent an upper bound for future optimization. In either case, increasing Q can improve the SNR in NQR experiments. For Johnson-noise–limited detection, $SNR_J \propto \sqrt{Q}$ (Eq. 5). If the noise floor is not yet limited by Johnson noise, as in our experiments (section S9b), SNR $\propto Q$ because M_{eff} still scales linearly with Q (Eq. 3). However, in both cases, higher Q is likely to result in a longer recovery time, which is problematic for some applications (*25*, *31*, *68*). Ultimately, the benefits of the resonant-induction amplification method are limited, as the SNR upper bound is the same for both diamond RF magnetometer and inductive coil detection, and the method may not be compatible with remote detection.

Sensor comparison for remote standoff detection

For remote NQR detection, an optimized diamond RF magnetometer is more likely to offer a clear advantage over inductive coil detection. Consider the case where a low-Q RF excitation loop is located sufficiently far from the sample that resonant-induction

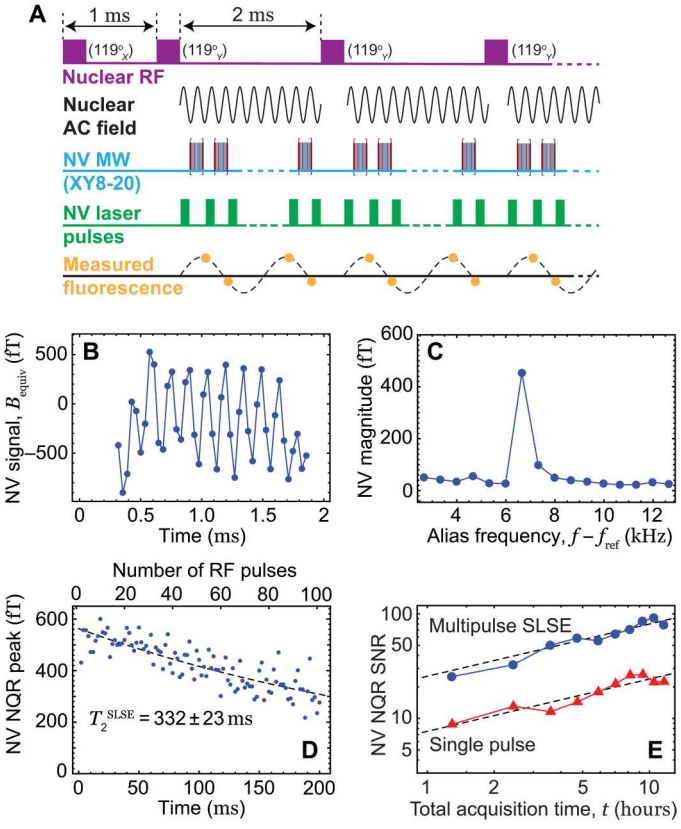

Fig. 6. SLSE NV NQR signal. (**A**) SLSE pulse sequence. Following an initial RF pulse, 100 echo pulses are applied every 2 ms. All RF pulses are applied at 3608 kHz for 50 μs (α ≈ 119°), and the initial pulse has a 90° phase shift with respect to all the echo pulses. Meanwhile, a synchronized XY8-20 MW pulse sequence is applied to the NV centers, with f_{ref} = 3600.07 kHz. The entire sequence is repeated every second. No additional phase cycling was used. (**B**) Time-domain NV SLSE signal (coherent average of the first 20 echos) from the 21-g sample. (**C**) SLSE NQR spectrum obtained from the absolute value of the Fourier transform of data in (B). (**D**) SLSE signal magnitude as a function of the time passed since the first RF pulse. The fitted exponential decay constant is $T_2^{SLSE} = 332 \pm 23$ ms. (**E**) SNR of NV NQR signals as a function of total acquisition time, *t*, for both SLSE and single–RF pulse protocol. The dashed black lines are fits to a $\sqrt{t}$ dependence.

amplification can be neglected (section S9c). Suppose that the ferrite-cone diamond RF magnetometer in the present experiment was replaced by a Johnson-noise–limited coil of equivalent volume (V_c = 1.5 cm^3) with Q = 10. The equivalent magnetic sensitivity of such a sensor is η_J/Q = 8 fT$_{rms}$ Hz$^{-1/2}$ (see Eq. 4). An order-of-magnitude improvement in diamond RF magnetometer sensitivity would already provide a superior SNR. Such a device could find application as a noncontact detector of pharmaceutical compounds, such as synthetic opioids like fentanyl, which require high sensitivity and a short recovery time (*31*). Beyond NQR spectroscopy, our device may also be used in applications such as magnetic induction tomography (*69*, *70*), underwater communication (*71*, *72*), or the search for exotic spin interactions (*73*–*75*).

In summary, we demonstrated a broadband (0.07 to 3.62 MHz) ferrite-cone diamond RF magnetometer with a sensitivity of ~70 fT s$^{1/2}$ at 0.35 MHz. The magnetometer was used to detect the 3.6-MHz NQR signal of ^{14}N from room temperature $NaNO_2$ powder samples. The short recovery time in our device after RF excitation pulse, ~35 μs, may offer advantages over other sensitive magnetometers for NQR spectroscopy.

MATERIALS AND METHODS

Experimental apparatus

The apparatus used here, shown in Fig. 1A, was adapted from the one presented in (*3*). Here, we provide additional information, with a focus on the changes that were implemented for RF magnetometry. An acousto-optic modulator (AOM; Brimrose TEM-85-10-532), driven at 81 MHz by an RF signal generator (RF-Consultant, TPI-1001-B), is used to gate a continuous-wave 532-nm green laser beam (Lighthouse Photonics Sprout D-5W) and produce 12-μs laser pulses. Following the AOM, a half-wave plate (Thorlabs, WPH10ME-633) is used to adjust the laser beam's polarization. The laser beam is then focused onto the edge facet of a diamond membrane using a 1-inch-diameter aspheric condenser lens (numerical apperture, 0.79; Thorlabs, ACL25416U-B). The same condenser lens is used to collect the NV fluorescence. The fluorescence is spectrally filtered by a dichroic mirror (Thorlabs DMLP567R) and a 650-nm long-pass filter (Thorlabs, FELH0650). Last, it is focused onto the "fluorescence channel" of the photodetector using a 2-inch-diameter lens (Thorlabs, ACL50832U-B).

A two-channel balanced photodetector (Thorlabs, PDB210A) with a fixed gain G = 175 kV/A ≈ 1.1 × 10^{24} V/(photoelectron/s) and a 3-dB bandwidth of DC–1 MHz is used to record the NV fluorescence signal. A small portion of the laser beam is picked off before the condenser lens and is directed to the "laser channel" of the photodetector for balanced detection.

The laser beam's peak power is measured before the condenser lens (but after the pick-off) to be ~250 mW. We estimate the peak power entering the diamond to be ~200 mW, after taking into account the ~80% transmission of the aspheric condenser at 532-nm wavelength. Using a camera imaging system, the full width at half maximum spot diameter of the laser beam on the diamond face was estimated to be ~35 μm. The effective sensing volume, V_{sen}, is taken as the product of the excitation beam area, ~π × (35 μm/2)^2, and the optical path length in the diamond, ~300 μm.

A ~1-cm-thick rectangular aluminum shield with dimensions of 18.4 cm by 18.4 cm by 30.8 cm is placed around the magnetometer apparatus to reduce RF interference. A permanent magnet placed outside of the Al shield, ~65 cm above the ferrite cones, is used to compensate the laboratory's ambient magnetic field and to apply weak bias magnetic fields, B_0 = 2 μT to 15 μT, approximately along the z axis. A vector magnetometer (Twinleaf, VMR018) is used to map the bias magnetic field at the location of the cones. The field components along the x and y axes are minimized by moving the magnet around.

Temperature-controlled housing

To improve temperature stability during NQR measurements, a 0.5-inch-thick thermal insulation sheet was glued to the exterior walls of the aluminum shield housing. A temperature control device (Thorlabs, ITC4005) was used to control the temperature of a Peltier element that is thermally attached to the Al shield with the help of silicone thermal paste. The ambient temperature was measured with a thermistor located near the sample.

Diamond membrane processing

The diamond membrane used here was created from a natural-isotopic-abundance diamond substrate, grown by chemical vapor deposition, with an initial nitrogen concentration [N] ≈ 20 ppm. The diamond was irradiated with 2-MeV electrons at a dose of $\sim 10^{18}$ cm^{-2}, and then, it was annealed in a vacuum furnace at 800° to 1100°C to form NV centers. The diamond properties, irradiation, and annealing procedures are similar to that described in (*8*). The diamond was subsequently cut and polished into a (100)-oriented membrane with dimensions of ~300 μm by 300 μm by 35 μm. We estimated the NV density of our membrane by comparing its fluorescence brightness to that of a well-calibrated diamond membrane [cut from "S2" studied in (*76*)] of similar dimensions under similar conditions. S2 has an NV density of ~15 ppm, and the detected photocurrent in our membrane was approximately five times lower, so we conclude that our membrane has an NV density of approximately 3 ppm. However, this method of estimating NV density has a substantial uncertainty of at least a factor of 2.

Sample preparation

Sodium nitrite ($NaNO_2$) powder sample was purchased from Sigma-Aldrich (lot no. MKBX1577V). Plastic cylinder containers with ~1-mm wall thickness were assembled to hold the powder samples in the setup.

Supplementary Materials

This PDF file includes:

Sections S1 to S9
Figs. S1 to S9
Tables S1 to S3
References

REFERENCES AND NOTES

1. J. F. Barry, J. M. Schloss, E. Bauch, M. J. Turner, C. A. Hart, L. M. Pham, R. L. Walsworth, Sensitivity optimization for NV-diamond magnetometry. *Rev. Mod. Phys.* **92**, 15004 (2020).
2. J. F. Barry, M. J. Turner, J. M. Schloss, D. R. Glenn, Y. Song, M. D. Lukin, H. Park, R. L. Walsworth, Optical magnetic detection of single-neuron action potentials using quantum defects in diamond. *Proc. Natl. Acad. Sci. U.S.A.* **113**, 14133–14138 (2016).
3. I. Fescenko, A. Jarmola, I. Savukov, P. Kehayias, J. Smits, J. Damron, N. Ristoff, N. Mosavian, V. M. Acosta, Diamond magnetometer enhanced by ferrite flux concentrators. *Phys. Rev. Res.* **2**, 23394 (2020).
4. E. R. Eisenach, J. F. Barry, M. F. O'Keeffe, J. M. Schloss, M. H. Steinecker, D. R. Englund, D. A. Braje, Cavity-enhanced microwave readout of a solid-state spin sensor. *Nat. Commun.* **12**, 1357 (2021).
5. C. Zhang, F. Shagieva, M. Widmann, M. Kübler, V. Vorobyov, P. Kapitanova, E. Nenasheva, R. Corkill, O. Rhrle, K. Nakamura, H. Sumiya, S. Onoda, J. Isoya, J. Wrachtrup, Diamond magnetometry and gradiometry towards subpicotesla dc field measurement. *Phys. Rev. Appl.* **15**, 064075 (2021).
6. Y. Masuyama, K. Mizuno, H. Ozawa, H. Ishiwata, Y. Hatano, T. Ohshima, T. Iwasaki, M. Hatano, Extending coherence time of macro-scale diamond magnetometer by dynamical decoupling with coplanar waveguide resonator. *Rev. Sci. Instrum.* **89**, 125007 (2018).
7. D. R. Glenn, D. B. Bucher, J. Lee, M. D. Lukin, H. Park, R. L. Walsworth, High-resolution magnetic resonance spectroscopy using a Solid-State spin sensor. *Nature* **555**, 351–354 (2018).
8. J. Smits, J. T. Damron, P. Kehayias, A. F. McDowell, N. Mosavian, I. Fescenko, N. Ristoff, A. Laraoui, A. Jarmola, V. M. Acosta, Two-dimensional nuclear magnetic resonance spectroscopy with a microfluidic diamond quantum sensor. *Sci. Adv.* **5**, eaaw7895 (2019).
9. Z. Wang, F. Kong, P. Zhao, Z. Huang, P. Yu, Y. Wang, F. Shi, J. Du, Picotesla magnetometry of microwave fields with diamond sensors. *Sci. Adv.* **8**, eabq8158 (2022).
10. S. T. Alsid, J. M. Schloss, M. H. Steinecker, J. F. Barry, A. C. Maccabe, G. Wang, P. Cappellaro, D. A. Braje, A solid-state microwave magnetometer with picotesla-level sensitivity. arXiv:2206.15440 [quant-ph] (2022).
11. I. M. Savukov, S. J. Seltzer, M. V. Romalis, K. L. Sauer, Tunable atomic magnetometer for detection of radio-frequency magnetic fields. *Phys. Rev. Lett.* **95**, 063004 (2005).
12. M. P. Ledbetter, V. M. Acosta, S. M. Rochester, D. Budker, S. Pustelny, V. V. Yashchuk, Detection of radio-frequency magnetic fields using nonlinear magneto-optical rotation. *Phys. Rev. A* **75**, 023405 (2007).
13. W. C. Griffith, S. Knappe, J. Kitching, Femtotesla atomic magnetometry in a microfabricated vapor cell. *Opt. Express* **18**, 27167–27172 (2010).
14. W. Wasilewski, K. Jensen, H. Krauter, J. J. Renema, M. V. Balabas, E. S. Polzik, Quantum noise limited and entanglement-assisted magnetometry. *Phys. Rev. Lett.* **104**, 133601 (2010).
15. J. E. Dhombridge, N. R. Claussen, J. Iivanainen, P. D. D. Schwindt, High-sensitivity rf detection using an optically pumped comagnetometer based on natural-abundance rubidium with active ambient- field cancellation. *Phys. Rev. Appl.* **18**, 044052 (2022).
16. W. Chalupczak, R. M. Godun, S. Pustelny, W. Gawlik, Room temperature femtotesla radio-frequency atomic magnetometer. *Appl. Phys. Lett.* **100**, 242401 (2012).
17. D. A. Keder, D. W. Prescott, A. W. Conovaloff, K. L. Sauer, An unshielded radio-frequency atomic magnetometer with sub-femtoTesla sensitivity. *AIP Adv.* **4**, 127159 (2014).
18. J. Clarke, Advances in SQUID magnetometers. *IEEE Trans. Electron Devices* **27**, 1896–1908 (1980).
19. M. Schmelz, V. Zakosarenko, A. Chwala, T. Schönau, R. Stolz, S. Anders, S. Linzen, H.-G. Meyer, Thin-film-based ultralow noise SQUID magnetometer. *IEEE Trans. Appl. Supercond.* **26**, 1600804 (2016).
20. J.-H. Storm, P. Hömmen, D. Drung, R. Körber, An ultra-sensitive and wideband magnetometer based on a superconducting quantum interference device. *Appl. Phys. Lett.* **110**, 072603 (2017).
21. Z.-H. Li, T.-Y. Wang, Q. Guo, H. Guo, H.-F. Wen, J. Tang, J. Liu, Enhancement of magnetic detection by ensemble NV color center based on magnetic flux concentration effect. *Acta Phys. Sin.* **70**, 147601 (2021).
22. Y. Xie, C. Xie, Y. Zhu, K. Jing, Y. Tong, X. Qin, H. Guan, C.-K. Duan, Y. Wang, X. Rong, J. Du, T_2-limited dc quantum magnetometry via flux modulation. arXiv:2204.07343 [quant-ph] (2022).
23. J. M. Taylor, P. Cappellaro, L. Childress, L. Jiang, D. Budker, P. R. Hemmer, A. Yacoby, R. Walsworth, M. D. Lukin, High-sensitivity diamond magnetometer with nanoscale resolution. *Nat. Phys.* **4**, 810–816 (2008).
24. C. Connor, J. Chang, A. Pines, Magnetic resonance spectrometer with a dc SQUID detector. *Rev. Sci. Instrum.* **61**, 1059–1063 (1990).
25. M. P. Augustine, D. M. TonThat, J. Clarke, SQUID detected NMR and NQR. *Solid State Nucl. Magn. Reson.* **11**, 139–156 (1998).
26. S. K. Lee, K. L. Sauer, S. J. Seltzer, O. Alem, M. V. Romalis, Subfemtotesla radio-frequency atomic magnetometer for detection of nuclear quadrupole resonance. *Appl. Phys. Lett.* **89**, 214106 (2006).
27. T. Das, E. Hahn, *Nuclear Quadrupole Resonance Spectroscopy* (Academic Press, 1958).
28. D. B. Zax, A. Bielecki, K. W. Zilm, A. Pines, D. P. Weitekamp, Zero field NMR and NQR. *J. Chem. Phys.* **83**, 4877–4905 (1985).
29. A. N. Garroway, M. L. Buess, J. B. Miller, B. H. Suits, A. D. Hibbs, G. A. Barrall, R. Matthews, L. J. Burnett, Remote sensing by nuclear quadrupole resonance. *IEEE Trans. Geosci. Remote Sens.* **39**, 1108–1118 (2001).
30. Y. J. Kim, T. Karaulanov, A. N. Matlashov, S. Newman, A. Urbaitis, P. Volegov, J. Yoder, M. A. Espy, Polarization enhancement technique for nuclear quadrupole resonance detection. *Solid State Nucl. Magn. Reson.* **61-62**, 35–38 (2014).
31. M. W. Malone, M. A. Espy, S. He, M. T. Janicke, R. F. Williams, The ^1H T^1 dispersion curve of fentanyl citrate to identify NQR parameters. *Solid State Nucl. Magn. Reson.* **110**, 101697 (2020).
32. E. Balchin, D. J. Malcolme-Lawes, I. J. F. Poplett, M. D. Rowe, J. A. S. Smith, G. E. S. Pearce, S. A. C. Wren, Potential of nuclear quadrupole resonance in pharmaceutical analysis. *Anal. Chem.* **77**, 3925–3930 (2005).
33. J. Lužnik, J. Pirnat, V. Jazbinšek, Z. Lavrič, S. Srčič, Z. Trontelj, The influence of pressure in paracetamol tablet compaction on ^{14}N nuclear quadrupole resonance signal. *Appl. Magn. Reson.* **44**, 735–743 (2013).
34. G. Kyriakidou, A. Jakobsson, K. Althoefer, J. Barras, Batch-specific discrimination using nuclear quadrupole resonance spectroscopy. *Anal. Chem.* **87**, 3806–3811 (2015).
35. D. L. Lyfar, V. E. Goncharuk, S. M. Ryabchenko, Temperature dependence of nuclear quadrupole resonance in layer-type crystals. *Phys. Status Solidi* **76**, 183–189 (1976).
36. S. Sharma, H. Paulus, N. Weiden, A. Weiss, Crystal structure and single crystal ^{35}Cl NQR of 1,2-dichloro-3-nitrobenzene, $Cl^{(1)}Cl^{(2)}(NO_2)^{(3)}C_6H_3$. *Z. Naturforsch. A* **41**, 134–140 (1986).
37. K. Horiuchi, T. Shimizu, H. Iwafune, T. Asaji, D. Nakamura, Temperature dependences of NQR frequencies and nuclear quadrupole relaxation times of chlorine in 2, 6-lutidinium

hexachlorotellurate(IV) as studied by pulsed NQR techniques. *Z. Naturforsch.* **45**, 485–489 (1990).
38. M. Huebner, J. Leib, G. Eska, NQR on gallium single crystals for absolute thermometry at very low temperatures. *J. Low Temp. Phys.* **114**, 203–230 (1999).
39. G. Lang, H.-J. Grafe, D. Paar, F. Hammerath, K. Manthey, G. Behr, J. Werner, B. Büchner, Nanoscale electronic order in iron pnictides. *Phys. Rev. Lett.* **104**, 097001 (2010).
40. M. W. Malone, G. A. Barrall, M. A. Espy, M. C. Monti, D. A. Alexson, J. K. Okamitsu, Polarization enhanced nuclear quadrupole resonance with an atomic magnetometer, in *Detection and Sensing of Mines, Explosive Objects, Obscured Targets XXI*, S. S. Bishop and J. C. Isaacs, Eds. (SPIE, 2016), vol. 9823, pp. 98230Z.
41. I. Lovchinsky, J. D. Sanchez-Yamagishi, E. K. Urbach, S. Choi, S. Fang, T. I. Andersen, K. Watanabe, T. Taniguchi, A. Bylinskii, E. Kaxiras, P. Kim, H. Park, M. D. Lukin, Magnetic resonance spectroscopy of an atomically thin material using a single-spin qubit. *Science* **355**, 503–507 (2017).
42. J. Henshaw, P. Kehayias, M. Saleh Ziabari, M. Titze, E. Morissette, K. Watanabe, T. Taniguchi, J. I. A. Li, V. M. Acosta, E. S. Bielejec, M. P. Lilly, A. M. Mounce, Nanoscale solid-state nuclear quadrupole resonance spectroscopy using depth-optimized nitrogen-vacancy ensembles in diamond. *Appl. Phys. Lett.* **120**, 174002 (2022).
43. C. S. Shin, M. C. Butler, H. J. Wang, C. E. Avalos, S. J. Seltzer, R. B. Liu, A. Pines, V. S. Bajaj, Optically detected nuclear quadrupolar interaction of ^{14}N in nitrogen-vacancy centers in diamond. *Phys. Rev. B Condens. Matter Mater. Phys.* **89**, 205202 (2014).
44. T. Oja, R. A. Marino, P. J. Bray, ^{14}N nuclear quadrupole resonance in the ferroelectric phase of sodium nitrite. *Phys. Lett. A* **26**, 11–12 (1967).
45. G. Petersen, P. J. Bray, ^{14}N nuclear quadrupole resonance and relaxation measurements of sodium nitrite. *J. Chem. Phys.* **64**, 522–530 (1976).
46. National Magnetics Group Inc., *High Permeability Mn-Zn Ferrite* (National Magnetics Group Inc., 2019).
47. T. Bolton, "Optimal design of electrically-small loop antenna including surrounding medium effects," thesis, Georgia Institute of Technology (2016).
48. G. Fisher, E. MacNamara, R. E. Santini, D. Raftery, A versatile computer-controlled pulsed nuclear quadrupole resonance spectrometer. *Rev. Sci. Instrum.* **70**, 4676 (1999).
49. N. Hiblot, B. Cordier, M. Ferrari, A. Retournard, D. Grandclaude, J. Bedet, S. Leclerc, D. Canet, A fully homemade ^{14}N quadrupole resonance spectrometer. *C. R. Chim.* **11**, 568–579 (2008).
50. B. H. Suits, Nuclear quadrupole resonance spectroscopy, in *Handbook of Applied Solid State Spectroscopy*, D. R. Vij Ed. (Springer, 2006), pp. 65–96.
51. M. Bloom, E. L. Hahn, B. Herzog, Free magnetic induction in nuclear quadrupole resonance. *Phys. Rev.* **97**, 1699–1709 (1955).
52. L. Qiu, Y. Zhang, H.-J. Krause, A. I. Braginski, A. Usoskin, High-temperature superconducting quantum interference device with cooled LC resonant circuit for measuring alternating magnetic fields with improved signal-to-noise ratio. *Rev. Sci. Instrum.* **78**, 054701 (2007).
53. M. Greer, D. Ariando, M. Hurlimann, Y. Q. Song, S. Mandal, Analytical models of probe dynamics effects on NMR measurements. *J. Magn. Reson.* **327**, 106975 (2021).
54. S. Vega, Theory of T_1 relaxation measurements in pure nuclear quadrupole resonance for spins / = 1. *J. Chem. Phys.* **61**, 1093–1100 (1974).
55. R. J. Cooper, D. W. Prescott, P. Matz, K. L. Sauer, N. Dural, M. V. Romalis, E. L. Foley, T. W. Kornack, M. Monti, J. Okamitsu, Atomic magnetometer multisensor array for rf interference mitigation and unshielded detection of nuclear quadrupole resonance. *Phys. Rev. Appl.* **6**, 064014 (2016).
56. R. A. Marino, S. M. Klainer, Multiple spin echoes in pure quadrupole resonance. *J. Chem. Phys.* **67**, 3388–3389 (1977).
57. R. S. Cantor, J. S. Waugh, Pulsed spin locking in pure nuclear quadrupole resonance. *J. Chem. Phys.* **73**, 1054–1063 (1980).
58. M. M. Maricq, Quasistationary state and its decay to equilibrium in the pulsed spin locking of a nuclear quadrupole resonance. *Phys. Rev. B* **33**, 4501–4513 (1986).
59. M. W. Malone, M. McGillvray, K. L. Sauer, Revealing dipolar coupling with NQR off-resonant pulsed spin locking. *Phys. Rev. B* **84**, 214430 (2011).
60. H. Clevenson, M. E. Trusheim, C. Teale, T. Schröder, D. Braje, D. Englund, Broadband magnetometry and temperature sensing with a light-trapping diamond waveguide. *Nat. Phys.* **11**, 393–397 (2015).
61. L. Xu, H. Yuan, N. Zhang, J. Zhang, G. Bian, P. Fan, M. Li, C. Zhang, Y. Zhai, J. Fang, High-efficiency fluorescence collection for NV- center ensembles in diamond. *Opt. Express* **27**, 10787–10797 (2019).
62. D. Le Sage, L. M. Pham, N. Bar-Gill, C. Belthangady, M. D. Lukin, A. Yacoby, R. L. Walsworth, Efficient photon detection from color centers in a diamond optical waveguide. *Phys. Rev. B* **85**, 121202 (2012).
63. H. Zhou, J. Choi, S. Choi, R. Landig, A. M. Douglas, J. Isoya, F. Jelezko, S. Onoda, H. Sumiya, P. Cappellaro, H. S. Knowles, H. Park, M. D. Lukin, Quantum metrology with strongly interacting spin systems. *Phys. Rev. X* **10**, 31003 (2020).
64. N. Arunkumar, K. S. Olsson, J. T. Oon, C. Hart, D. B. Bucher, D. Glenn, M. D. Lukin, H. Park, D. Ham, R. L. Walsworth, "Quantum logic enhanced sensing in solid-state spin ensembles. arXiv:2203.12501 [quant-ph] (2022).
65. S.-K. Lee, M. V. Romalis, Calculation of magnetic field noise from high-permeability magnetic shields and conducting objects with simple geometry. *J. Appl. Phys.* **103**, 084904 (2008).
66. Y. J. Kim, I. Savukov, Ultra-sensitive magnetic microscopy with an optically pumped magnetometer. *Sci. Rep.* **6**, 24773 (2016).
67. D. Hoult, R. Richards, The signal-to-noise ratio of the nuclear magnetic resonance experiment. *J. Magn Reson* **24**, 71–85 (1976).
68. C. M. Verber, H. P. Mahon, W. H. Tanttila, Nuclear resonance of aluminum in synthetic ruby. *Phys. Rev.* **125**, 1149–1157 (1962).
69. G. Chatzidrosos, A. Wickenbrock, L. Bougas, H. Zheng, O. Tretiak, Y. Yang, D. Budker, Eddy-current imaging with nitrogen-vacancy centers in diamond. *Phys. Rev. Appl.* **11**, 14060 (2019).
70. L. M. Rushton, T. Pyragius, A. Meraki, L. Elson, K. Jensen, Unshielded portable optically pumped magnetometer for the remote detection of conductive objects using eddy current measurements. *Rev. Sci. Instrum.* **93**, 125103 (2022).
71. V. Gerginov, F. C. S. da Silva, D. Howe, Prospects for magnetic field communications and location using quantum sensors. *Rev. Sci. Instrum.* **88**, 125005 (2017).
72. C. Deans, L. Marmugi, F. Renzoni, Active underwater detection with an array of atomic magnetometers. *Appl. Optics* **57**, 2346–2351 (2018).
73. D. F. Jackson Kimball, J. Dudley, Y. Li, S. Thulasi, S. Pustelny, D. Budker, M. Zolotorev, Magnetic shielding and exotic spin-dependent interactions. *Phys. Rev. D* **94**, 82005 (2016).
74. P.-H. Chu, N. Ristoff, J. Smits, N. Jackson, Y. J. Kim, I. Savukov, V. M. Acosta, Proposal for the search for new spin interactions at the micrometer scale using diamond quantum sensors. *Phys. Rev. Res.* **4**, 23162 (2022).
75. H. Liang, M. Jiao, Y. Huang, P. Yu, X. Ye, Y. Wang, Y. Xie, Y.-F. Cai, X. Rong, J. Du, New constraints on exotic spin-dependent interactions with an ensemble-NV-diamond magnetometer. *Natl. Sci. Rev.*, nwac262 (2022).
76. V. M. Acosta, E. Bauch, M. P. Ledbetter, C. Santori, K. M. Fu, P. E. Barclay, R. G. Beausoleil, H. Linget, J. F. Roch, F. Treussart, S. Chemerisov, W. Gawlik, D. Budker, Diamonds with a high density of nitrogen-vacancy centers for magnetometry applications. *Phys. Rev. B* **80**, 115202 (2009).
77. A. Gregorovi˘, T. Apih, Relaxation during spin-lock spin-echo pulse sequence in N14 nuclear quadrupole resonance. *J. Chem. Phys.* **129**, 214504 (2008).

Acknowledgments: The authors acknowledge advice and support from J. Damron, M. Aiello, A. Berzins, M. Saleh Ziabari, A. M. Mounce, D. Budker, I. Savukov, and M. Conradi. Y.S. can be contacted at yaser.silani@gmail.com. **Funding:** This work was funded by NSF award CHE-1945148 and NIH awards DP2GM140921, R41GM145129, and R21EB027405. Research presented in this presentation was also supported, in part, by the Laboratory Directed Research and Development program of Los Alamos National Laboratory under project number 20220086DR. Los Alamos National Laboratory is operated by Triad National Security LLC, for the National Nuclear Security Administration of the U.S. Department of Energy (contract no. 89233218CNA000001). I.F. acknowledges support from Latvian Council of Science project lzp-2021/1-0379. **Competing interests:** A.J. is a cofounder of ODMR Technologies and has financial interests in the company. A.F.M. is the founder of NuevoMR LLC and has financial interests in the company. The authors declare that they have no other competing interests. **Author contributions:** V.M.A., Y.S., and I.F. conceived the idea for the study in consultation with A.J., P.K., and M.W.M. Y.S. carried out simulations, performed experiments, and analyzed the data with guidance from J.S. and V.M.A. I.F., M.W.M., A.F.M., A.J., B.A.R., N.M., and N.R. contributed to experimental design and data analysis. All authors discussed results and helped write the paper. **Data and materials availability:** All data needed to evaluate the conclusions in the paper are present in the paper and/or the Supplementary Materials.

Submitted 24 February 2023
Accepted 10 May 2023
Published 16 June 2023
10.1126/sciadv.adh3189